Electronic Supplementary Material (ESI) for Journal of Materials Chemistry A.

Supporting Information

High Performance Duckweed-derived Carbon Support to Anchor NiFe Electrocatalysts for Efficient Solar Energy Driven Water Splitting

Ashwani Kumar, Dhirendra K. Chaudhary, Sahanaz Parvin and Sayan Bhattacharyya*

Department of Chemical Sciences, and Centre for Advanced Functional Materials, Indian Institute of Science Education and Research (IISER) Kolkata, Mohanpur - 741246, India

*Email for correspondence: sayanb@iiserkol.ac.in

Field Emission Scanning Electron Microscopy (FESEM), Transmission Electron Microscopy (TEM), X-ray Diffraction (XRD) Pattern, Surface Area Analysis and Current-Voltage (I-V) characteristics

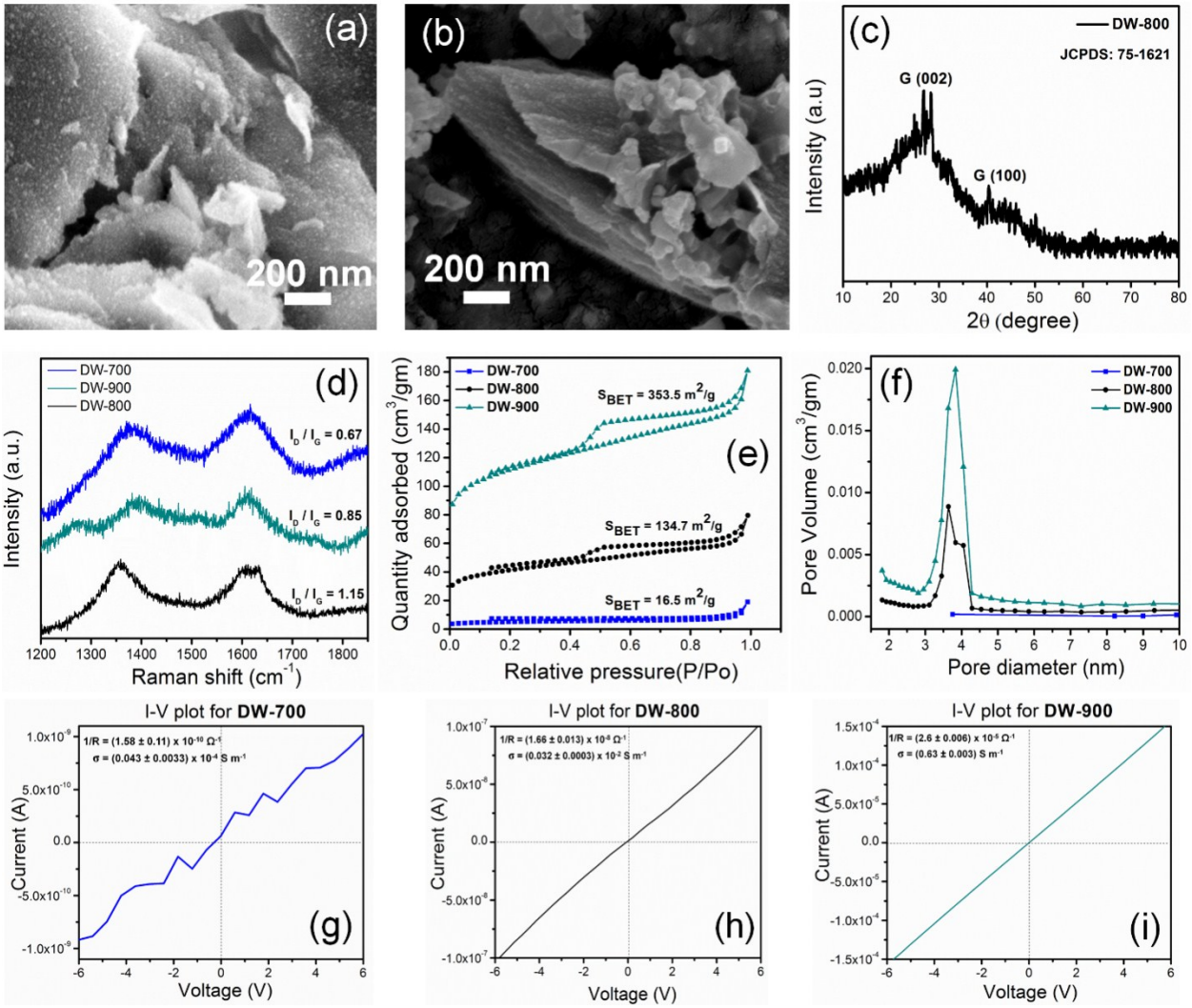

Fig. S1 FESEM images of (a) pre-carbonized duckweed and (b) DW-800. (c) XRD pattern of DW-800. (d-f) Raman spectra, N_2 adsorption-desorption isotherms, and pore size distribution profile, respectively, of DW samples synthesized at three different temperatures (700, 800 and 900). (g-i) Current-voltage (I-V) plots of DW-700, DW-800, and DW-900, respectively.

Energy Dispersive Analysis of X-rays (EDAX)

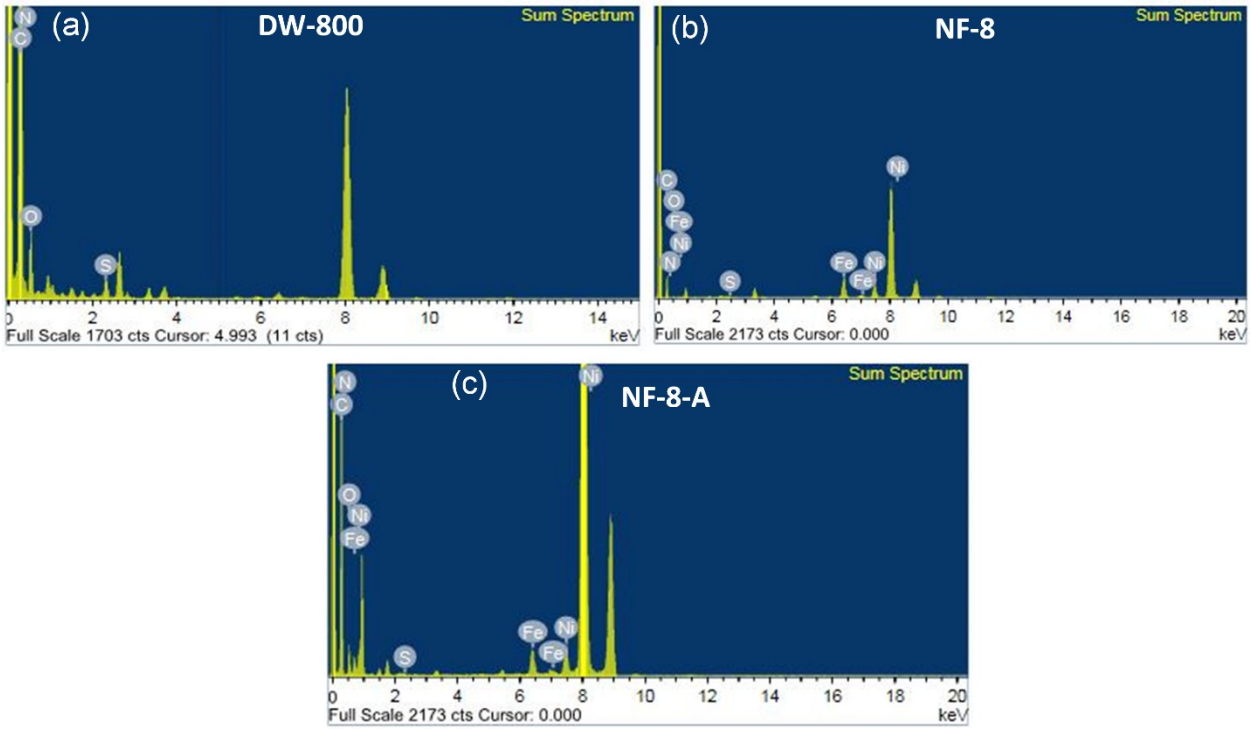

Fig. S2 EDAX patterns of (a) DW-800, (b) NF-8 and (c) NF-8-A.

Table S1. BET surface area and pore characteristics of different samples.

Samples	S_{BET} ($m^2\ g^{-1}$)	V_{Total} ($cm^3\ g^{-1}$)	Average Pore diameter (nm)
NF-8-A	225	0.13	3.8 (Sharp)
NF-8-Annealed-900	198.9	0.12	3.8 (Sharp)
NF-9	64.1	0.07	3.8 (Sharp)
NF-8	116.5	0.08	3.74 (Sharp)
NF-7	36.2	0.03	3.9 (Sharp)
NF-8 (1:2)	67.9	0.05	3.8 (Sharp)
NF-8 (2:1)	42.7	0.04	3.8 (Sharp)
DW-900	353.5	0.16	4.7 (Sharp)
DW-800	134.7	0.08	5.6 (Sharp)
DW-700	16.5	0.02	15-36 (Broad)
1:1 Ni:Fe-800	7	0.08	8-20 (Broad)

X-ray Diffraction (XRD)

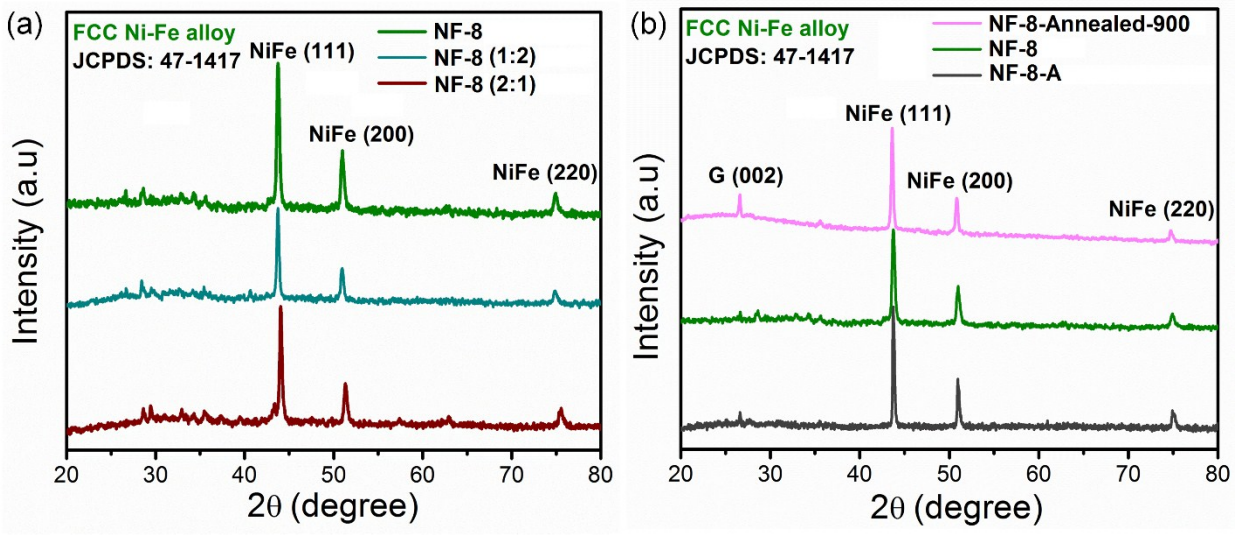

Fig. S3 XRD patterns of (a) duckweed samples with different compositions of Ni and Fe, and (b) NF-8-Annealed-900 and NF-8-A.

Enlarged View of G (002) Reflection

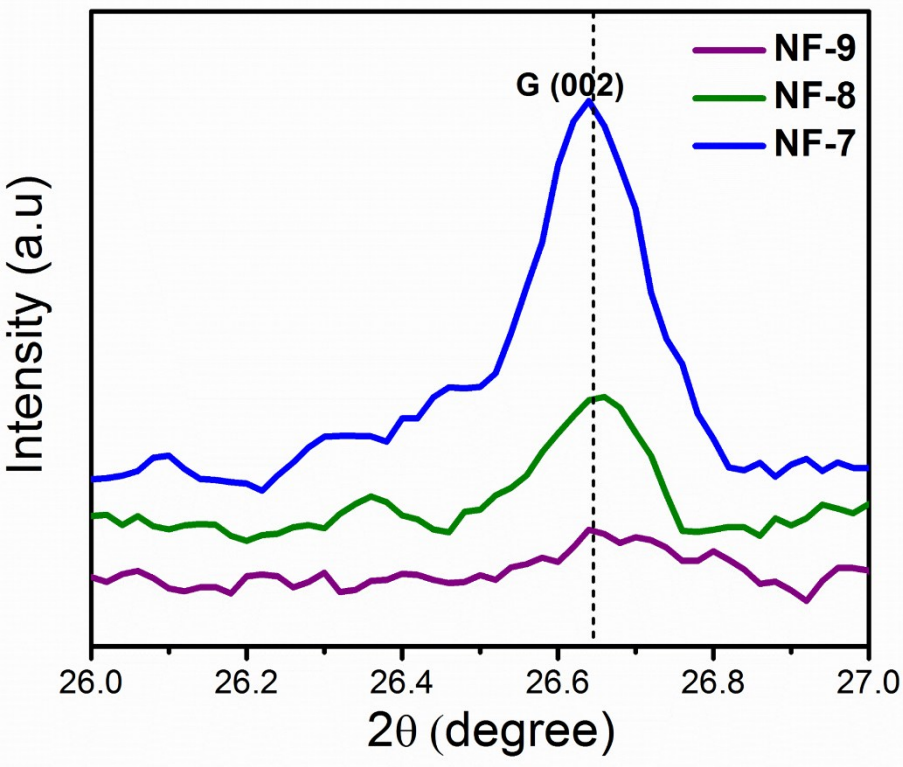

Fig. S4 Zoom in XRD patterns of Figure 2a at 2θ = 26-27° for NF-7, NF-8 and NF-9 samples.

X-ray photoelectron spectroscopy (XPS)

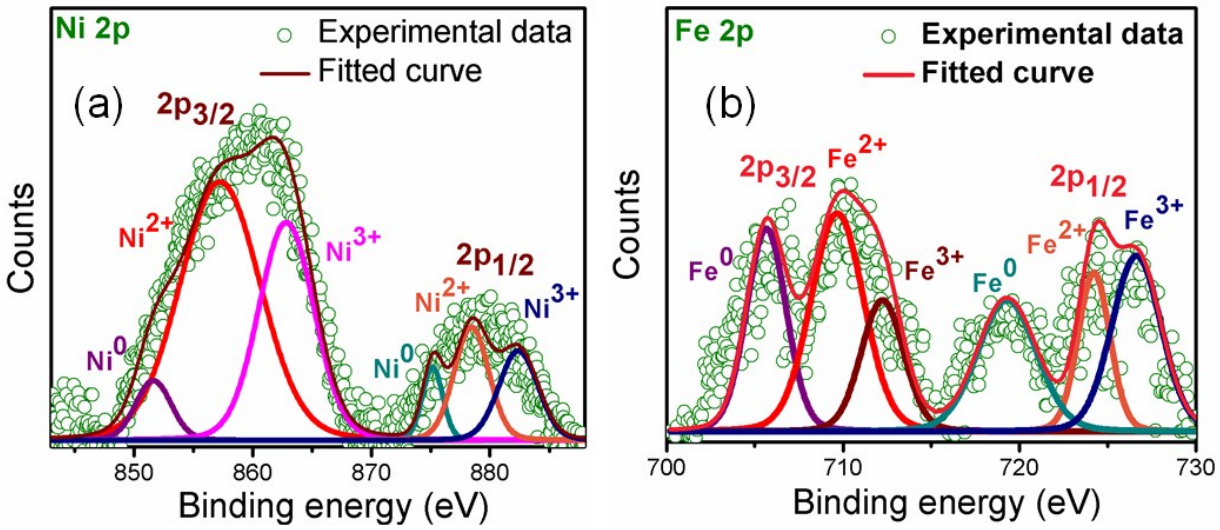

Fig. S5 High-resolution fitted XPS spectrum of (a) Ni *2p* and (b) Fe *2p* in NF-8.

The XPS data are corrected with respect to C *1s* spectra. The fitted plots show that Ni $2p_{3/2}$ can be deconvoluted into three sub-peaks consisting of Ni^0, Ni^{2+} and Ni^{3+} at binding energies 851.6, 857.3 and 862.8 eV, respectively.[S1] Similarly, in the Fe $2p_{3/2}$ spectra, the three sub-peaks at binding energies of 705.7, 709.7 and 712.3 eV correspond to Fe^0, Fe^{2+} and Fe^{3+}, respectively.[S2] Since XPS is a surface phenomenon, the existence of higher oxidation states along with the metallic NiFe core is mainly due to surface oxidation.[S3]

Table S2. Molar ratio of Ni/Fe obtained from EDAX, averaged over multiple locations.

Sample	Ni (Atomic %)	Fe (Atomic %)	Ni : Fe	
			Expected	Observed
NF-9	31.87	32.11	1:1	0.99:1
NF-8	21.35	21.93	1:1	0.97:1
NF-7	5.75	5.36	1:1	1.07:1
NF-8 (1:2)	12.36	23.4	1:2	1:1.89
NF-8 (2:1)	34.83	18.99	2:1	1.83:1
NF-8-Annealed-900	4.37	4.45	1:1	0.98:1
NF-8-A	6.88	6.62	1:1	1.03:1
1:1 Ni:Fe-800	18.48	17.79	1:1	1.04:1

Table S3. Weight % of carbon to metal in different samples.

Sample	Carbon (Weight %)	Ni (Weight %)	Fe (Weight %)
NF-9	65	18.17	16.83
NF-8	66.39	17.4	16.2
NF-7	62.62	19.82	17.56
NF-8 (1:2)	63.3	13.4	23.3
NF-8 (2:1)	68.12	20.06	11.93
NF-8-Annealed-900	68.45	16.02	15.53
NF-8-A	62.06	20.35	17.59

Surface Area Analysis

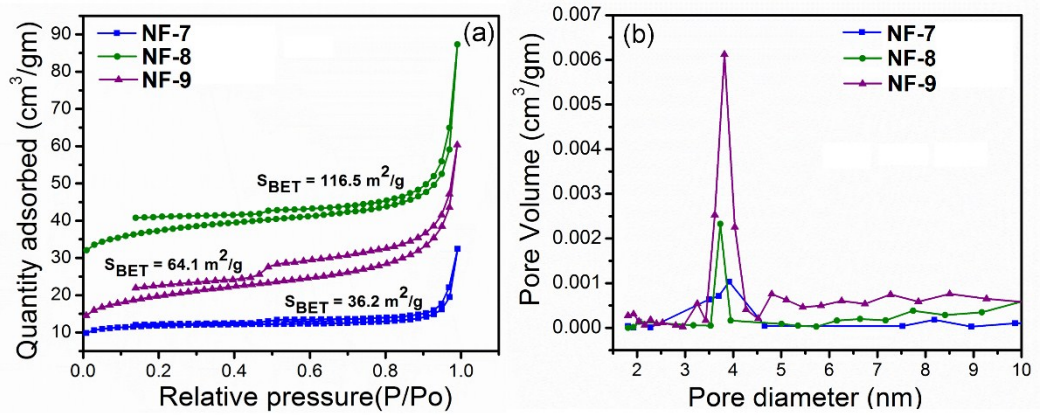

Fig. S6 (a) Nitrogen adsorption-desorption isotherms and (b) corresponding pore size distribution profiles, respectively, for NF-7, NF-8 and NF-9.

Current-Voltage (I-V) characteristics

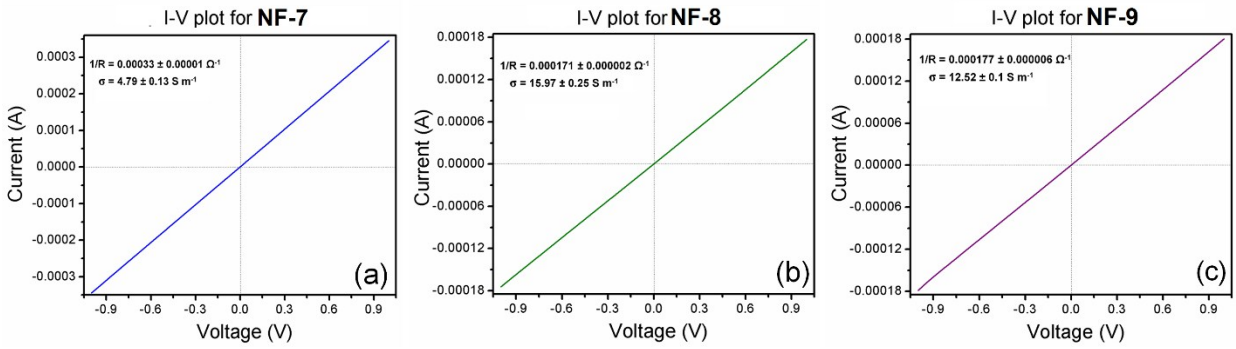

Fig. S7 Current-Voltage (I-V) characteristic curves of (a) NF-7, (b) NF-8 and (c) NF-9, respectively.

Field Emission Scanning Electron Microscopy (FESEM) images

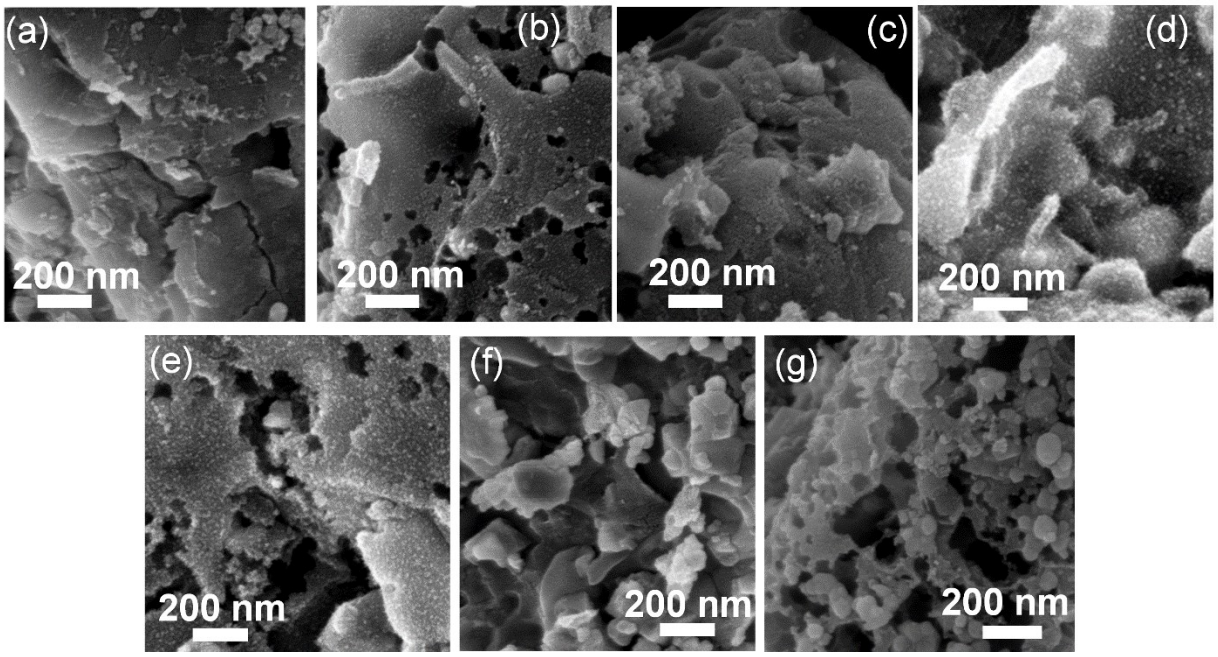

Fig. S8 FESEM images of (a) NF-7, (b) NF-8, (c) NF-9, (d) NF-8-Annealed-900, (e) NF-8-A, (f) NF-8 (1:2) and (g) NF-8 (2:1).

Raman Spectra

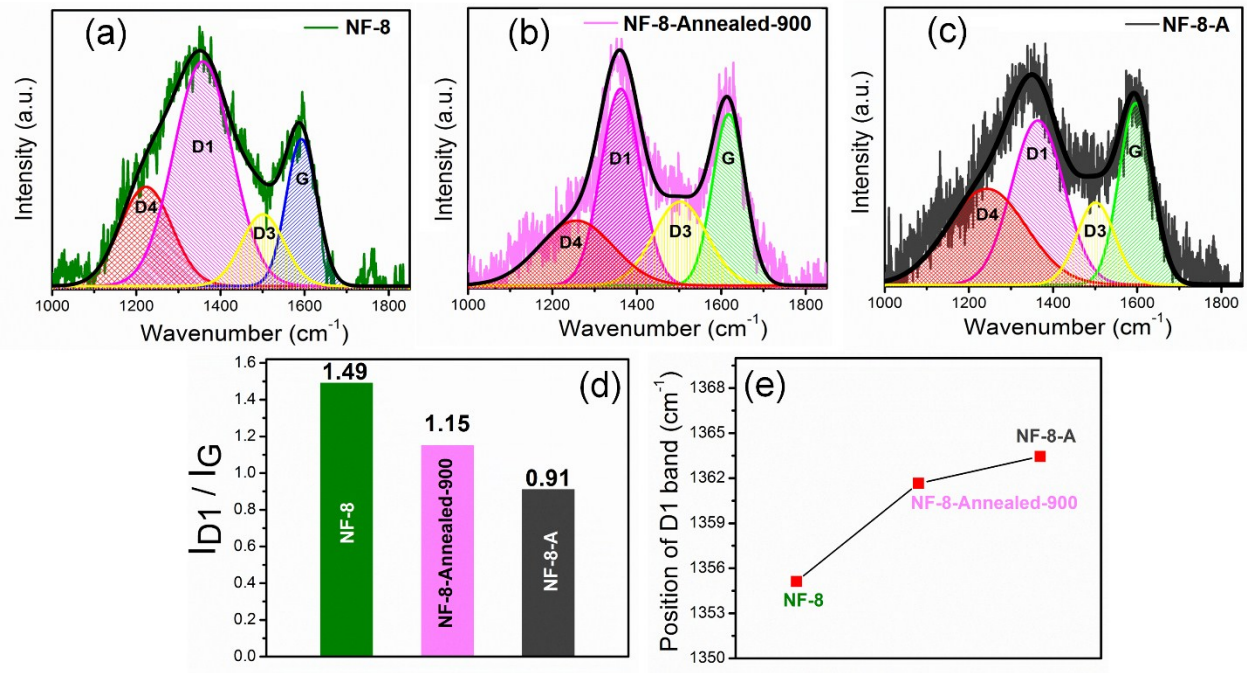

Fig. S9 Fitted Raman spectra of (a) NF-8, (b) NF-8-Annealed-900 and (c) NF-8-A. (d) Relative intensity and (e) position of D1 defect band.

Table S4. Elemental quantification of carbon, nitrogen, sulfur, nickel, iron and oxygen in different samples by EDAX.

Sample	C (Atomic %)	Ni (Atomic %)	Fe (Atomic %)	N (Atomic %)	S (Atomic %)	O (Atomic %)
DW-800	96.3	-	-	0.6	0.33	2.77
NF-8	78.09	8.04	8.56	0.9	0.27	4.14
NF-8-A	89.28	2.14	2.08	0.33	0.07	6.1

Surface Area Analysis

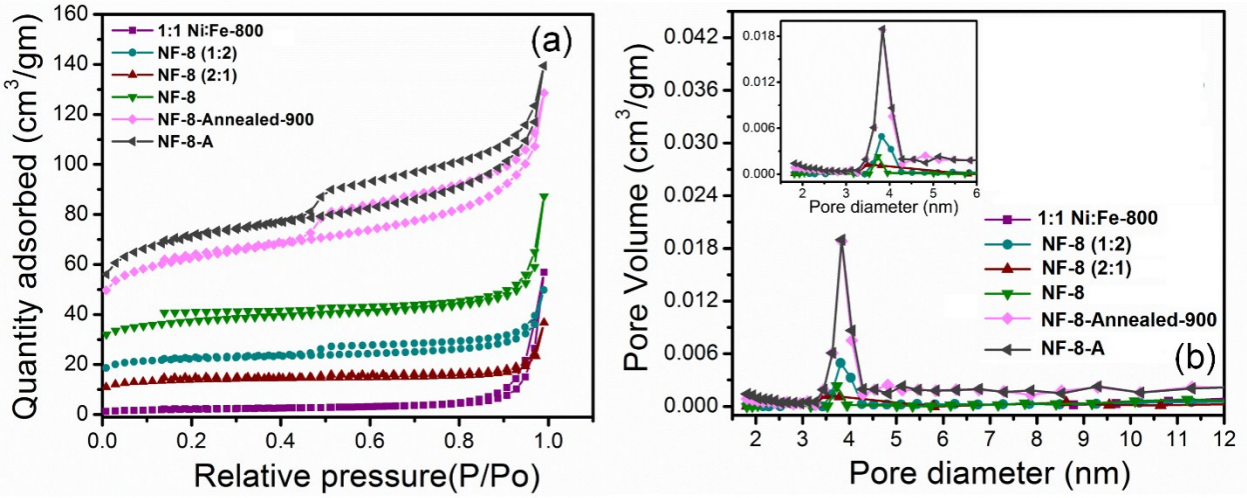

Fig. S10 (a) Nitrogen adsorption-desorption isotherms and (b) corresponding pore size distribution profiles for NF-8, NF-8 (1:2), NF-8 (2:1), 1:1 Ni:Fe-800, NF-8-Annealed-900 and NF-8-A.

LSV Polarization Curves of Only Duckweed Samples

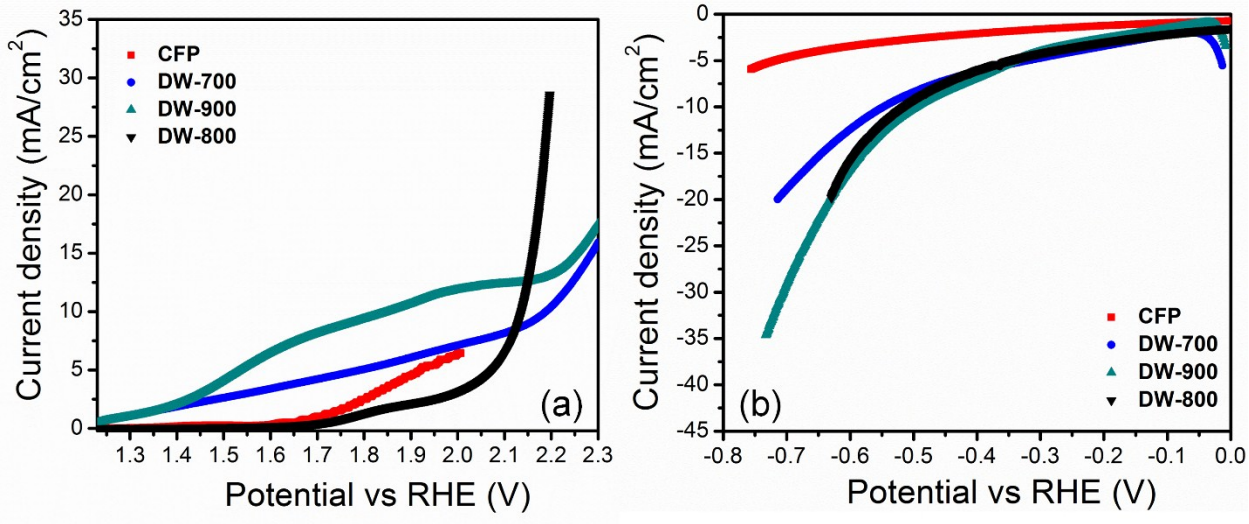

Fig. S11 LSV polarization curves for (a) OER and (b) HER, respectively for DW-700, DW-800, and DW-900.

LSV Polarization Curves with Different Catalyst Loading

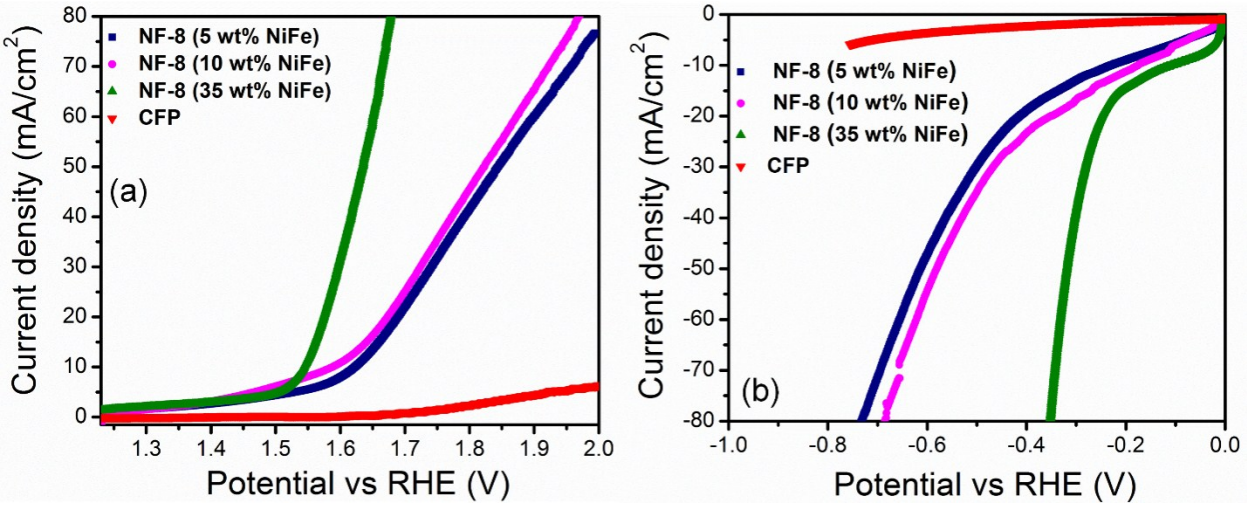

Fig. S12 LSV polarization curves for (a) OER and (b) HER, with different loading wt% of NF-8 catalyst.

LSV Polarization Curves in Optimizing the Calcination Temperature and Composition

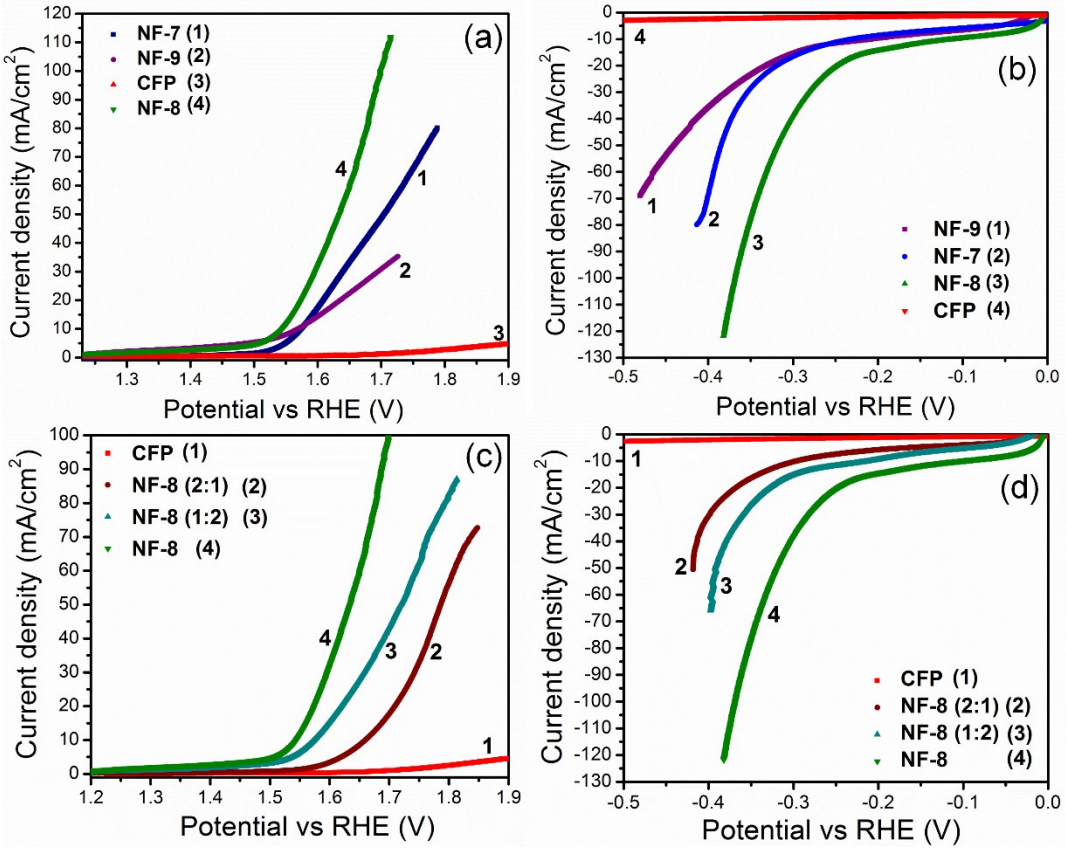

Fig. S13 LSV polarization curves for (a) OER and (b) HER with NF-7, NF-8 and NF-9 samples for optimizing the calcination temperature. LSV polarization curves for (c) OER and (d) HER of NF-8, NF-8 (1:2), and NF-8 (2:1) for composition optimization.

Polarization Curves for OER and HER of NF-8, NF-8-Annealed-900 and NF-8-A

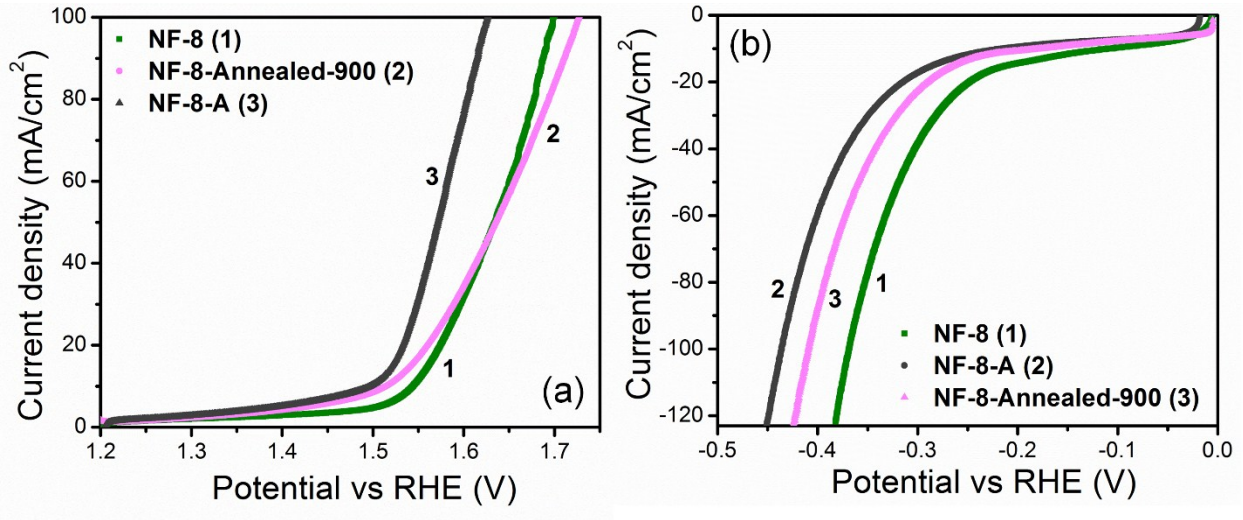

Fig. S14 LSV polarization curves for (a) OER and (b) HER with NF-8, NF-8-Annealed-900, and NF-8-A.

Activity Comparison with Bimetallic 1:1 Ni:Fe Alloy Nanoparticles

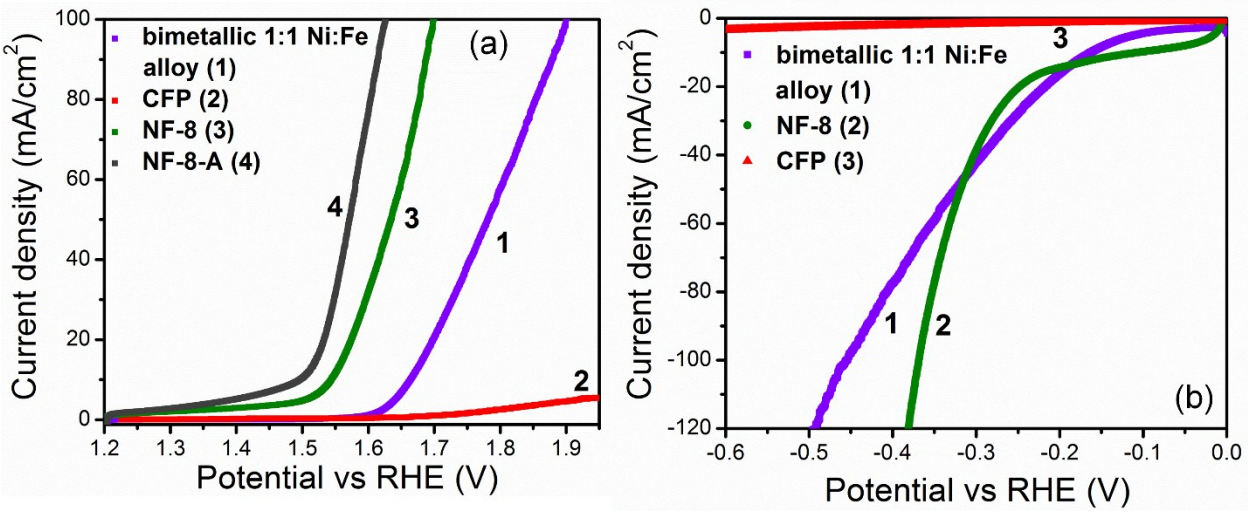

Fig. S15 LSV polarization curves for (a) OER and (b) HER. Activity comparison of NF-8 and NF-8-A, with bimetallic 1:1 Ni:Fe alloy.

Activity Comparison with RGO 1:1 NiFe-800

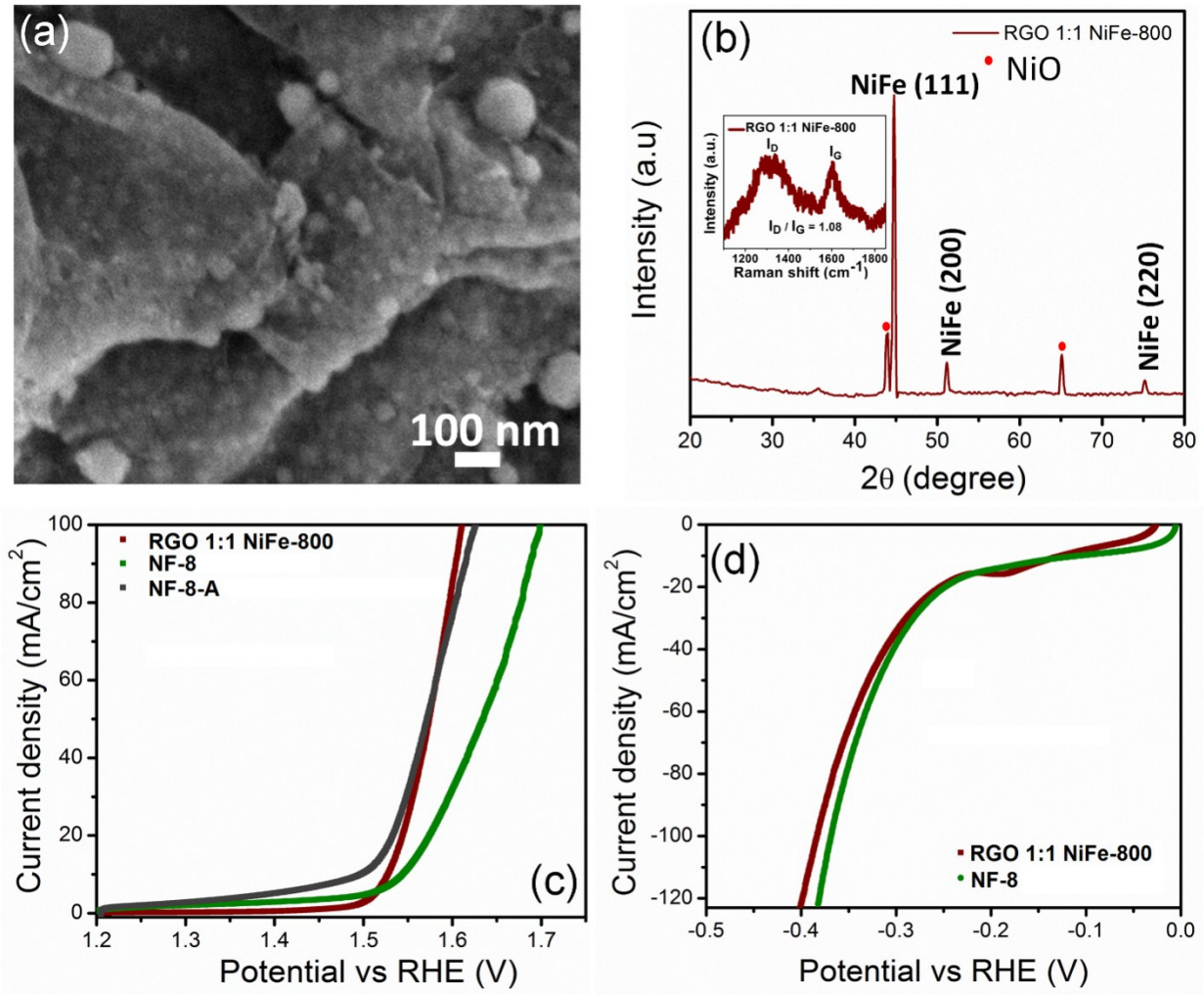

Fig. S16 (a) FESEM image of RGO 1:1 NiFe-800. (b) XRD pattern of RGO 1:1 NiFe-800. Inset shows the Raman spectrum. LSV polarization curves for (c) OER and (d) HER. Activity comparison of NF-8 and NF-8-A, with RGO 1:1 NiFe-800.

The FESEM image in Fig. S16a shows that the NiFe nanoparticles are uniformly distributed on the reduced graphene oxide sheets. The XRD pattern and the Raman spectrum in Fig. S16b confirm the formation of NiFe-alloy nanoparticles on graphitic carbon structure.

Activity Comparison on Glassy Carbon Electrode

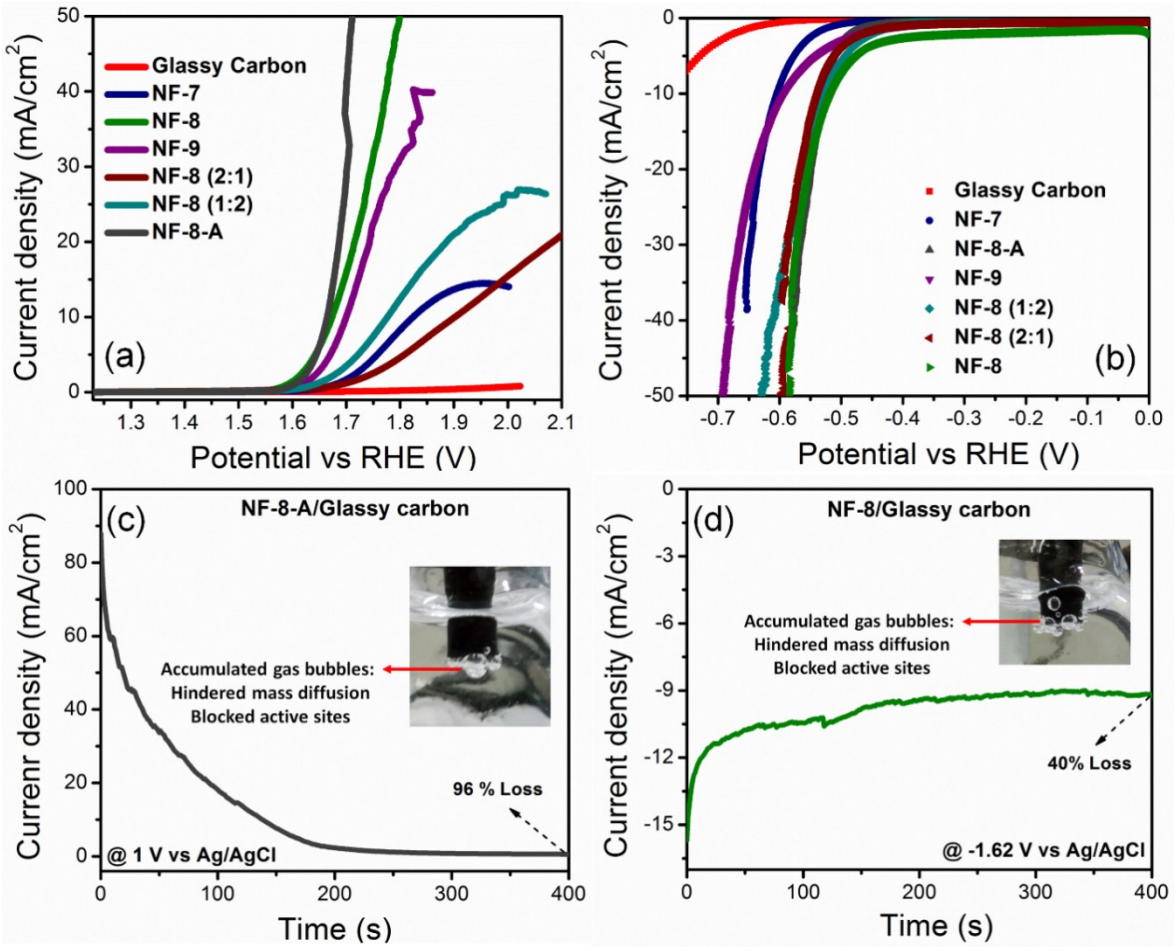

Fig. S17 LSV polarization curves for (a) OER and (b) HER, on glassy carbon electrode. Stability tests of (c) NF-8-A/Glassy carbon for OER and (d) NF-8/Glassy carbon for HER. Insets show the optical images of accumulated gas bubbles.

With a low catalyst loading of 0.5 mg cm^{-2} on 2D glassy carbon electrode, NF-8-A and NF-8 show the best activity for OER and HER, respectively. However the activity is less than that compared to the catalyst on 3D CFP (Fig. S17 a, b). This is due to the poor contact of the catalyst NPs with the glassy carbon electrode hampering electron flow, bubble accumulation on the catalyst surface hindering mass diffusion of the reactants and products as well as blocking the active sites of the catalyst by nafion binder.

In fact, stability of the catalysts is also very poor on the glassy carbon electrode which is due to the accumulated gas bubbles and blocked active sites which is one of the prime reasons for not using glassy carbon electrode as a catalyst support for industrial scale hydrogen production (Fig. S17 c, d).

Electrochemical Impedance Spectroscopy (EIS) Tests

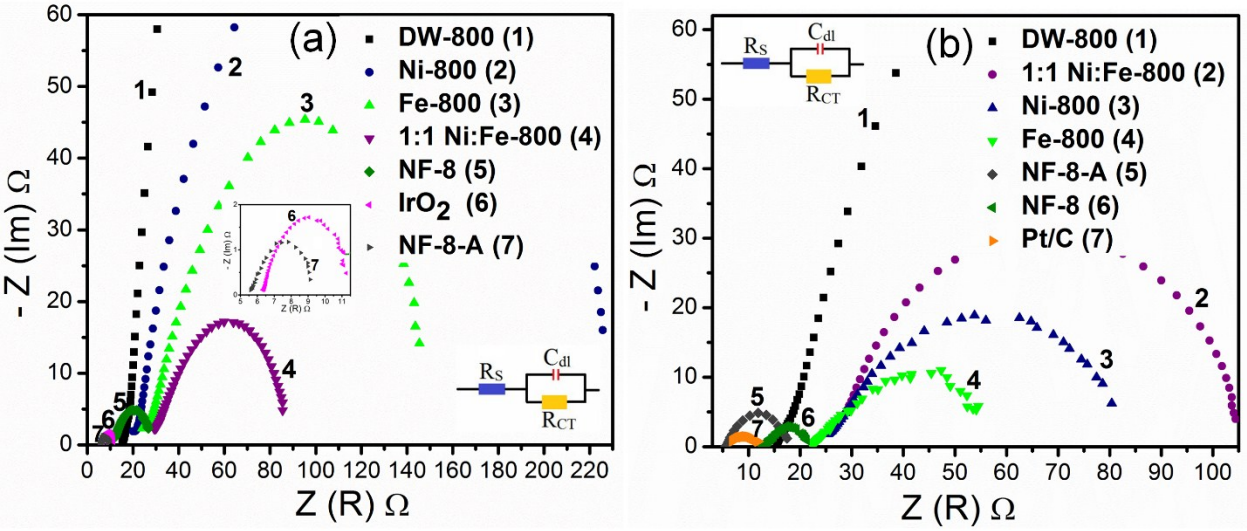

Fig. S18 Nyquist plots obtained by EIS at (a) 372 mV overpotential for OER and (b) 398 mV overpotential for HER (*iR* uncorrected).

Cyclic Voltammograms (CVs) and Current Density at Different Scan Rates for C_{dl} Estimation

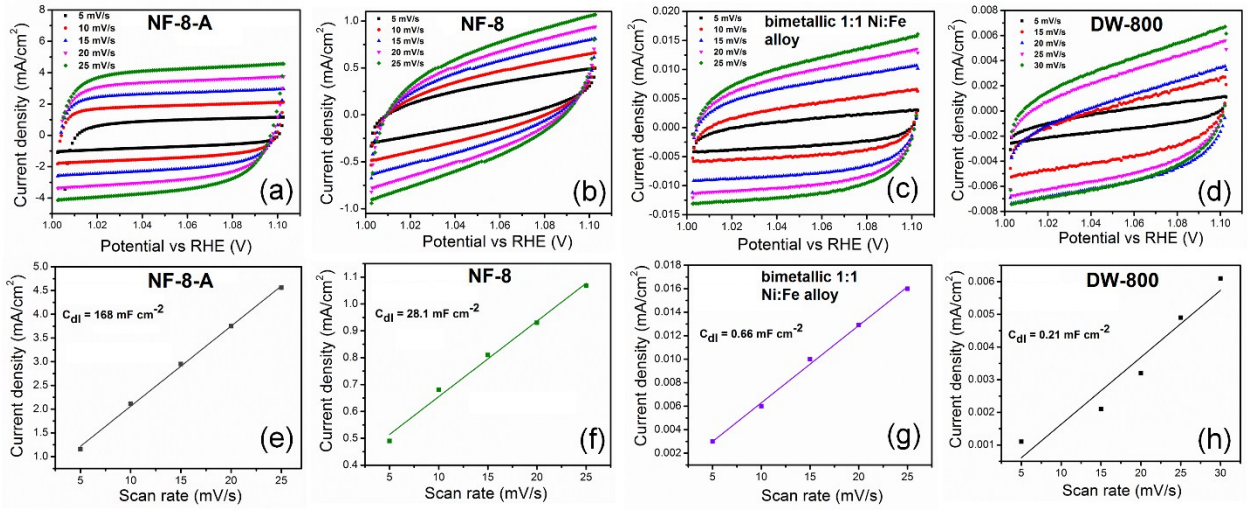

Fig. S19 CV plots of (a) NF-8-A, (b) NF-8, (c) bimetallic 1:1 Ni:Fe alloy and (d) DW-800, at different scan rates. Current density (recorded at a fixed potential) as a function of scan rate for (e) NF-8-A, (f) NF-8, (g) bimetallic 1:1 Ni:Fe alloy and (h) DW-800.

XRD and TEM Analysis of Electrocatalysts after Stability Test

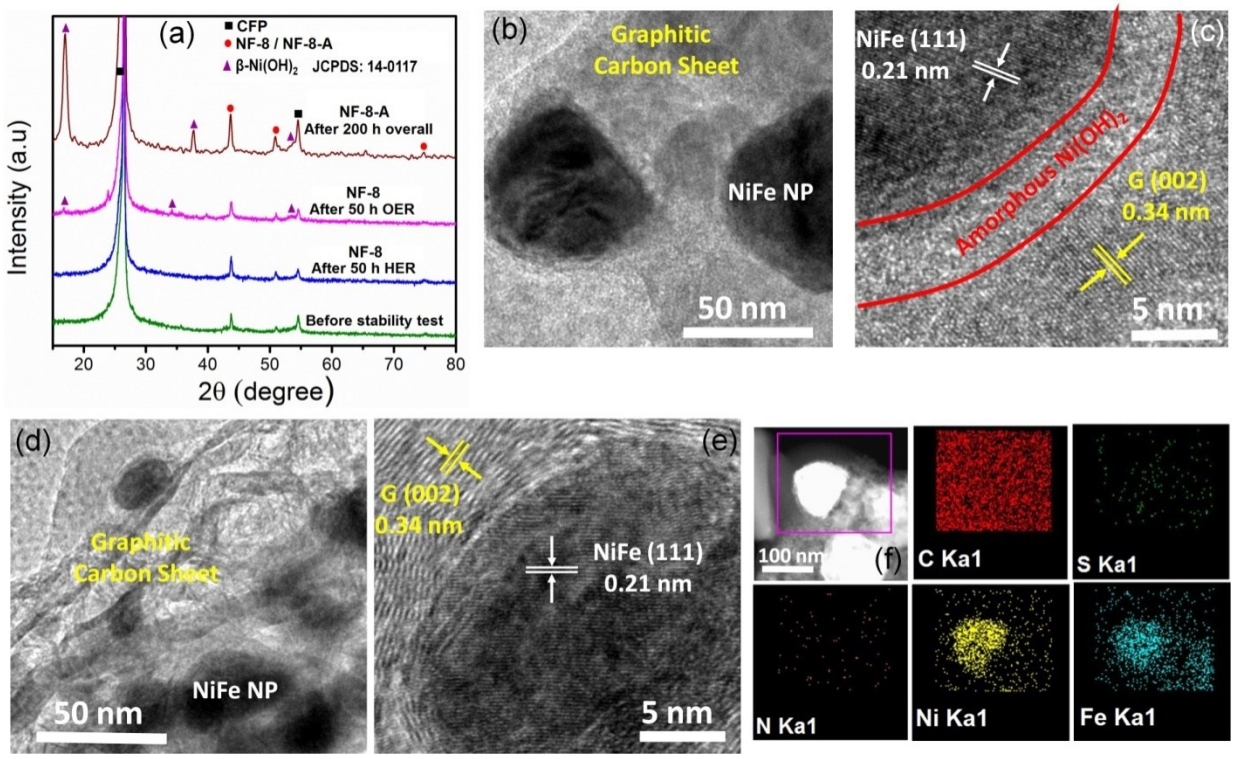

Fig. S20 (a) XRD patterns of as-prepared catalysts/CFP; NF-8/CFP after 50 h of OER and HER stability tests and NF-8-A/CFP (anode) after 200 h of overall stability test. (b) TEM and (c) HRTEM images of NF-8-A. (d) TEM and (e) HRTEM images of NF-8, after 200 h overall stability test. (f) STEM-HAADF image with the corresponding elemental maps of NF-8-A, after 200 h overall stability test.

Comparison of the HER Activity of NF-8 with Graphite and Pt Rod Counter Electrodes

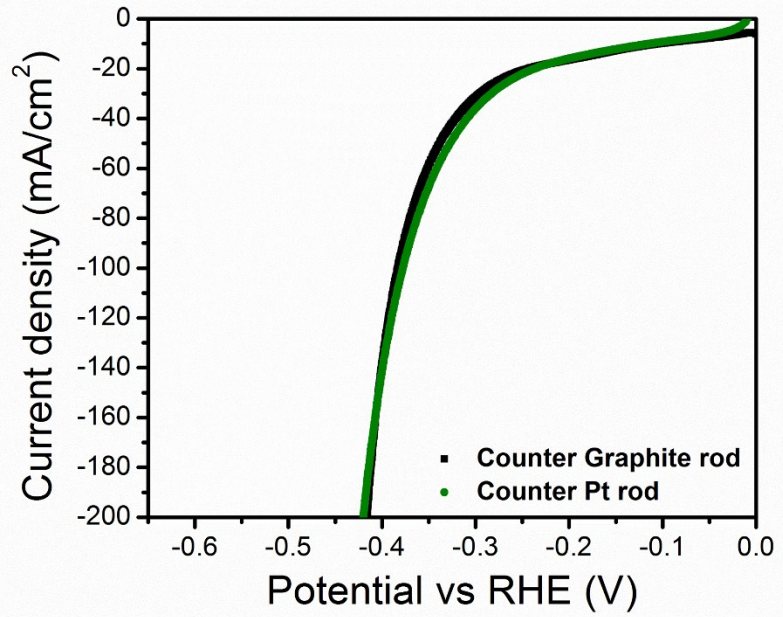

Fig. S21 Polarization curves of NF-8 for HER by using graphite rod (black curve) and Pt rod (olive curve) as the counter electrode.

Table S5. Comparison of the water splitting performance of catalysts in this work and other reported transition metal electrocatalysts in alkaline media.

Catalyst	η@10 mA cm^{-2} (HER) (mV)	(OER)		Cell Voltage @10 mA cm^{-2} (V)	Ref.
		η@10 mA cm^{-2} (mV)	η@20 mA cm^{-2} (mV)		
NF-8	106	314	344	NF-8 (-) ‖ NF-8-A (+) 1.61	This work
NF-8-A	215	267	303		
NiFe-NCs	197	271	295	1.67	S4
NiFe LDH/NF	210	240		1.7	S5
$Ni_{0.9}Fe_{0.1}$/NC/CFP	215 (GC)	330 (GC)		1.64	S6
CoP/GO-400	150	340		1.7	S7
Ni-Co-P hollow nanobricks	107	270		1.62	S8
NiFe-P nanocubes	182	271		1.68	S9
FeCo	149			FeCo (-)‖FeCoNi (+) 1.687	S10
FeCoNi		288			
Ni_3FeN/r-GO	94	270		1.60	S11
NiFeV/NF	125	231		1.591	S12
$Co_{5.47}N$ NP@N-PC	149	248		1.62	S13

Chronoamperometry Test of NF-8 (-) ‖ NF-8 (+) and Pt/C (-) ‖ IrO_2 (+) electrolyzers

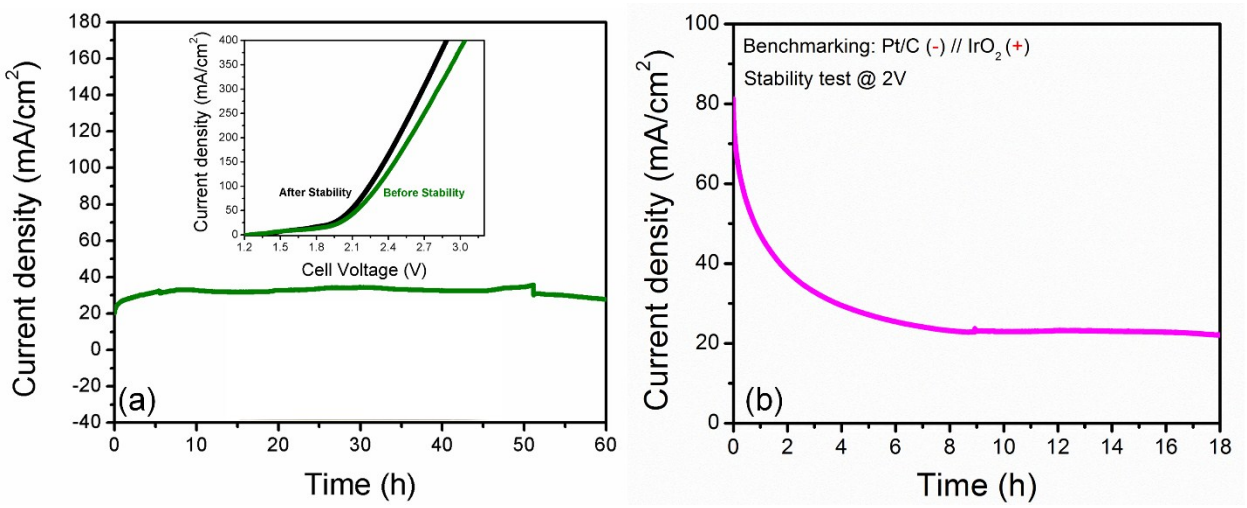

Fig. S22 Chronoamperometry tests of water electrolysis at a cell voltage of 2 V for (a) NF-8 (-) ‖ NF-8 (+) and (b) Pt/C (-) ‖ IrO_2 (+).

Table S6. Comparison table for the solar-to-hydrogen efficiency with other reports.

Electrolyzer	Solar cell	Power conversion efficiency of solar cell (PEC)	Cell Voltage of electrolzer @10 mA cm^{-2} (V)	Solar-to-hydrogen efficiency (η_{STH})	Ref.
NF-8 (-) ‖ NF-8-A (+)	Organic-inorganic halide perovskite	Single solar cell: 19.26 % Two integrated solar cell: 12.23 %	1.61	9.7 %	This work
NiFe-LDH (-) ‖NiFe-LDH (+)	Organic-inorganic halide perovskite	Single solar cell: 17.3 % Two integrated solar cell: 15.7 %	1.7	12.3 %	S5
Pt (-) ‖ Pt (+)	Triple junction polymer solar cell	5.3 %	1.7	3.1 %	S14
NiFeSP/NF (-) ‖ NiFeSP/NF (+)	Commercial planar Si solar cell	-	1.58	9.2 %	S15
NrGO/NCNTs (-) ‖ NrGO/NCNTs (+)	Organic-inorganic halide perovskite	Single solar cell: 14.89 % Two integrated solar cell: 11.28 %	1.72	9.02 %	S13

References

S1 J.Nsanzimana, Y.Peng, M. Miao, V.Reddu, W. Zhang, H. Wang, B. Xia and X. Wang,*ACS Appl. Nano Mater.*, 2018, **1**, 1228-1235.

S2 L. Martín-García, I. Bernal-Villamil, M. Oujja, E. Carrasco, R. Gargallo-Caballero, M. Castillejo, J. F. Marco, S.Gallego and J. Figuera, *J. Mater. Chem. C*, 2016, **4**, 1850-1859.

S3 A. Dutta and J. Datta, *J. Mater. Chem. A*, 2014, **2**, 3237-3250.

S4 A. Kumar and S. Bhattacharyya, *ACS Appl. Mater. Interfaces*, 2017, **9**, 41906.

S5 J. Luo, J. H. Im, M. T. Mayer, M. Schreier, M. K. Nazeeruddin, N. G. Park, S. D. Tilley, H. J. Fan and M. Grätzel, *Science*, 2014, **345**, 1593.

S6 X. Zhang, H. Xu, X. Li, Y. Li, T. Yang and Y. Liang, *ACS Catal.*, 2016, **6**, 580.

S7 L. Jiao, Y. X. Zhou and H. L. Jiang, *Chem. Sci*., 2016, **7**, 1690.

S8 E. Hu, Y. Feng, J. Nai, D. Zhao, Y. Hu and X. W. D. Lou, *Energy Environ. Sci.*, 2018, **11**, 872.

S9 C. Xuan, J. Wang, W. Xia, Z. Peng, Z. Wu, W. Lei, K. Xia, H. L. Xin and D. Wang, *ACS Appl. Mater. Interfaces*, 2017, **9**, 26134.

S10 Y. Yang, Z. Lin, S. Gao, J. Su, Z. Lun, G. Xia, J. Chen, R. Zhang and Q. Chen, *ACS Catal.*, 2017, **7**, 469.

S11 Y. Gu, S. Chen, J. Ren, Y. A. Jia, C. Chen, S. Komarneni, D. Yang and X. Yao, *ACS Nano.*, 2018, **12**, 245.

S12 K. N. Dinh, P. Zheng, Z. Dai, Y. Zhang, R. Dangol, Y. Zheng, B. Li, Y. Zong and Q. Yan, *Small*, 2018, **14**, 1703257.

S13 Z. Chen, Y. Ha, Y. Liu, H. Wang, H. Yang, H. Xu, Y. Li and R. Wu, *ACS Appl. Mater. Interfaces*, 2018, **10**, 7134.

S14 S. Esiner, H. V. Eersel, M. M. Wienk and R. A. J. Janssen, *Adv. Mater.*, 2013, **25**, 2932.

S15 Y. Xin, X. Kan, L. Y. Gan and Z. Zhang, *ACS Nano.*, 2017, **11**, 10303.

S16 A. R. Bin, M. Yusoff and J. Jang, *Chem. Commun.*, 2016, **52**, 5824.